

Vapor Deposition of Semiconducting Phosphorus Allotropes into TiO₂ Nanotube Arrays for Photoelectrocatalytic Water Splitting

Ebru Üzer,[†] Pawan Kumar,^{‡,§} Ryan Kisslinger,^{‡,§} Piyush Kar,[‡] Ujwal Kumar Thakur,[‡] Sheng Zeng,[‡] Karthik Shankar,^{*,‡} and Tom Nilges^{*,†}

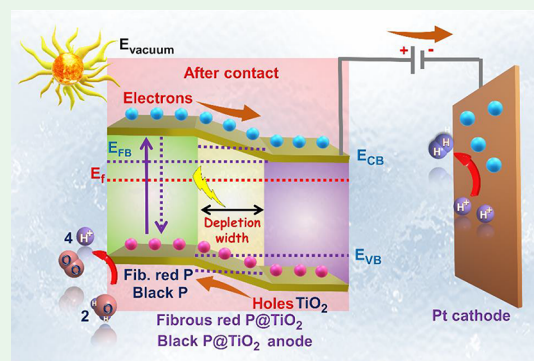
[†]Department of Chemistry, Technical University of Munich, Lichtenbergstrasse 4, Garching 85748, Germany

[‡]Department of Electrical and Computer Engineering, Faculty of Engineering, University of Alberta, 9211 116th Street NW, Edmonton, Alberta T6G 1H9, Canada

Supporting Information

ABSTRACT: Recent evidence of exponential environmental degradation will demand a drastic shift in research and development toward exploiting alternative energy resources such as solar energy. Here, we report the successful low-cost and easily accessible synthesis of hybrid semiconductor@TiO₂ nanotube photocatalysts. In order to realize its maximum potential in harvesting photons in the visible-light range, TiO₂ nanotubes have been loaded with earth-abundant, low-band-gap fibrous red and black phosphorus (P). Scanning electron microscopy– and scanning transmission electron microscopy–energy-dispersive X-ray spectroscopy, X-ray diffraction, Raman spectroscopy, X-ray photoelectron microscopy, and UV–vis measurements have been performed, substantiating the deposition of fibrous red and black P on top and inside the cavities of 100- μ m-long electrochemically fabricated nanotubes. The nanotubular morphology of titania and a vapor-transport technique are utilized to form heterojunctions of P and TiO₂. Compared to pristine anatase 3.2 eV TiO₂ nanotubes, the creation of heterojunctions in the hybrid material resulted in 1.5–2.1 eV photoelectrocatalysts. An enhanced photoelectrochemical water-splitting performance under visible light compared with the individual components resulted for the P@TiO₂ hybrids. This feature is due to synergistically improved charge separation in the heterojunction and more effective visible-light absorption. The electronic band structure and charge-carrier dynamics are investigated in detail using ultraviolet photoelectron spectroscopy and Kelvin probe force microscopy to elucidate the charge-separation mechanism. A Fermi-level alignment in P@TiO₂ heterojunctions leads to a more reductive flat-band potential and a deeper valence band compared to pristine P and thus facilitates a better water-splitting performance. Our results demonstrate effective conversion efficiencies for the nanostructured hybrids, which may enable future applications in optoelectronic applications such as photodetectors, photovoltaics, photoelectrochemical catalysts, and sensors.

KEYWORDS: phosphorus, TiO₂, vapor-phase deposition, low-band-gap materials, photocatalyst, heterojunction, sunlight-driven water splitting



INTRODUCTION

Limited reserves of carbon-emitting fossil fuels and their associated negative environmental impact have triggered research into finding alternative self-sustainable technologies. Sunlight-driven water splitting to generate hydrogen fuels is a promising approach as an alternate energy technology. However, photosplitting of water to generate hydrogen is unfavorable because of a high positive Gibbs free-energy change (+237 kJ mol⁻¹) and the need for a process requiring a photocatalyst (usually semiconductor) with appropriate conduction band (CB) and valence band (VB) positions.¹ Various nanostructured semiconductor materials have been extensively investigated for application in photochemical and photoelectrochemical water splitting, i.e., BiVO₄, WO₃, Fe₂O₃, MoS₂, CoO, g-C₃N₄, CdS, Ga_{1-x}Zn_xN_{1-x}O_x, SnS₂, SrTiO₃, etc.^{2–7} However, meeting the broad range of required

properties in one single material to actuate water splitting remains a challenge; such properties include visible-light absorptivity, long-lived charge carriers, high quantum efficiency, electrochemical resiliency, low cost, and nontoxicity with the appropriateness of the CB (<0.00 V vs NHE) and VB (>1.23 V vs NHE) edges for electron transfer and the formation of hydrogen (reduction) and oxygen from water (oxidation), respectively. TiO₂, which meets many of the aforementioned requirements, nevertheless suffers from poor visible-light absorption and fast recombination of photo-generated charge carriers. Band-structure manipulation of TiO₂ via approaches such as doping, sensitization, hetero-

Received: February 5, 2019

Accepted: May 9, 2019

Published: May 9, 2019

junction formation, etc., and morphological engineering are enticing approaches to improve the quantum efficiency.^{8–11} One-dimensional (1D) TiO₂ nanostructures like nanorods, nanotubes, nanocones, etc., are particularly interesting because of their large accessible surface areas, vectorial charge-transport pathways, and a carrier retrieval length comparable to that of the smallest dimension of the nanostructure. Thus, they have emerged as excellent candidates for heterojunction formation with low-band-gap semiconductors.^{12–17}

Low-cost TiO₂ nanotube layers fabricated via electrochemical anodization present varied applications in photocatalytic, photovoltaic, and optoelectronic sensing devices.^{18–20} By maximization of the specific surface area from bulk to nanoparticulate TiO₂, improvement of the photoelectrochemical water-splitting performance using solar light can be achieved.²¹ To broaden the application spectrum and overcome key drawbacks of TiO₂ nanotubes, our intention is band-gap engineering and semiconductor/electrolyte contact optimization, which play a major role in efficient photocatalytic water splitting.^{22,23} Therefore, we utilize a hybrid system of semiconductor materials between highly ordered self-organized TiO₂ nanotube membranes and inexpensive phosphorus (P) allotropes, 1D fibrous red P and two-dimensional (2D) black P, which leads to higher-efficiency composite photocatalysts. As-prepared hollow nanosized cylinders of TiO₂ nanotubes were formed by electrochemical, field-aided, three-step anodization of titanium (Ti) films or foils in electrolytes containing F⁻/I⁻/ClO₃⁻ ions. Both P allotropes were deposited via low-pressure chemical vapor deposition (CVD).^{24,25} In order to prevent the semiconductor–semiconductor hybrid from material degradation during long thermal treatment processes, the vapor deposition or so-called mineralization technique allows crystallization of amorphous TiO₂ to anatase. At the same time, the desirable growth of P nanorods inside and onto the nanotubes in one annealing step (at ~500 °C) takes place. The intrinsic band gap for the n-type semiconductor anatase TiO₂ in the UV range at 3.2 eV limits light absorption to only <5% of the solar spectrum.²⁶ To much better exploit the solar spectrum, heterojunction systems with two P allotropes were investigated: (a) fibrous red P, exhibiting a band gap of 2.25 eV based on our experimental results and (b) p-type semiconducting black P due to a direct band gap of 0.3 eV for bulk material in the near-IR region. The latter is characterized by a high, layer-dependent hole-carrier mobility of ca. 10⁵ cm²/(V s).^{27–29} Fibrous red P is being investigated regarding its potential as a water-splitting agent and black P as a field-effect transistor, a photodetector, and a sensor.^{30–32} In a heterojunction system, the photogenerated carrier mechanism can induce the formation of a built-in potential (V_{bi}) and hinder electron–hole pair recombination.^{33–36} The dense hybrid structure supports the fast charge separation of carriers, created inside the nanorods, and migration of a short distance equal to the nanotube radius to cross the heterojunction interface. Excellent quantum yields can be obtained from the suitable nanotube structure because of a high aspect ratio, which ensures efficient photon harvesting, orthogonalized processes of charge separation and light absorption, and improved light trapping by Mie scattering.^{37–39} Modification of the TiO₂ nanotubes has been approached by the decoration of surfaces with noble-metal nanoparticles, such as gold, silver, and platinum. A solid interface occurs, in which a Schottky contact is formed that is less preferable than a p/n-semiconductor contact in terms of charge-carrier recombin-

tion loss.^{23,38,40,41} Recently, the desired Z-scheme junction formation has been successfully carried out with CdS, g-C₃N₄, MoS₂, ZnIn₂S₄, Fe₂O₃, halide perovskites, etc., for use in extensive photocatalytic applications such as CO₂ photo-reduction, high-performance photoanodes for water-splitting devices, selective gas sensors, and high-efficiency solar cells.^{42–47} In this work, we introduce a vapor-transport process to grow hybrid semiconductor–semiconductor 1D and 2D materials to form heterojunctions capable of realizing enhanced photoelectrochemical water splitting.

RESULTS AND DISCUSSION

This section is divided into two main chapters: (1) structural characterization of fibrous red and black P deposited into and onto the TiO₂ nanotube arrays and (2) the photocatalytic activity of the P allotrope@TiO₂ hybrid materials. Spectroscopic [X-ray photoelectron spectroscopy (XPS), UV–vis, Raman, and Kelvin probe force microscopy (KPFM) studies in the Supporting Information, SI] and X-ray diffraction (XRD; see the SI) experiments were applied to characterize the bare and hybrid materials. A brief photoelectrocatalytic investigation of the P allotrope@TiO₂ hybrid materials contains the full electrochemical characterization [hydrogen and oxygen evolution and calculation of the efficiencies, i.e., ABPE, IPCE, APCE, and Faradaic efficiency (FE) in the SI], including a plausible mechanism for the water-splitting activity of the title compounds.

Structural Characterization of P Allotrope@TiO₂ Nanotube Hybrids. In order to fabricate hybrid semiconducting materials, we succeeded in filling the anatase-type TiO₂ nanotubes with fibrous red and black P using a short-way transport reaction (Figure 1; experimental details are given in

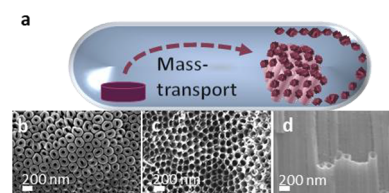


Figure 1. (a) Fibrous P (purple pellet) reacted onto and into TiO₂ nanotube membranes (pink). Representative SEM pictures of the electrochemically prepared TiO₂ nanotube membranes used in a mineralizer-driven short-way transport reaction along the (b) bottom, (c) top, and (d) normal side views.

the SI). This reaction is adapted from the so-called mineralization principle used for the synthesis of a plethora of P-containing compounds, as in fibrous solely, binary, and ternary P compounds like NaP₇ and SnIP.^{48–50}

The TiO₂ nanotube structure could be preserved after the deposition of P allotropes via thermal treatment during the transport reactions.

Fibrous Red P@TiO₂ Nanotubes. The mineralization method can be applied to prepare element allotropes and binary and ternary compounds. An example is the successful deposition of fibrous red P onto and into TiO₂ nanotube membranes via the gas phase, as shown in Figure 2. Pure fibrous P exhibits photocatalytic activity and has the potential for water-splitting applications.²⁰ Fibrous red P has been formed everywhere on the TiO₂ nanotube membrane (Figure 2b). Noticeably, fibrous P is distributed on the whole surface of the membranes, as scanning electron microscopy–energy-

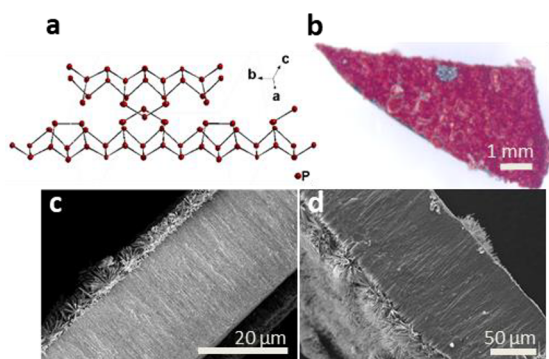


Figure 2. (a) Crystal structure of fibrous red P. (b) TiO₂ nanotube membrane covered with fibrous red P after reaction via gas phase. (c and d) SEM images of the cross section and surface of fibrous P@TiO₂ nanotube membranes. Fibrous P covers the surface of the membrane. EDS of the cross section shows P all along the nanotubes (Table S1).

dispersive X-ray spectroscopy (SEM–EDS) measurements exhibit in Figure 2c,d and Table S1. According to powder XRD data, the growth of fibrous red P on top of the TiO₂ nanotube membranes was confirmed (Figure S1).

Scanning transmission electron microscopy (STEM) images taken after separation of the TiO₂ nanotubes by an ultrasonication process show a bundle of nanotubes with diameters of ~90–100 nm. Elemental mapping confirms Ti, oxygen (O), and P with a distribution of P along the full tube length (Figure 3).

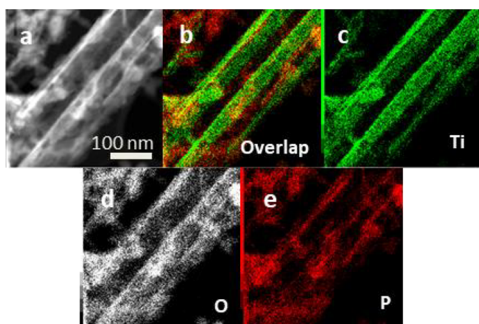


Figure 3. (a) STEM bright-field image of TiO₂ nanotubes separated from a membrane by an ultrasonication procedure. (b) Elemental mapping of the overlaid elements Ti, O, and P. (c and d) Ti and O of the TiO₂ nanotubes, (e) with P distributed along the full length of the tubes.

The successful growth of a fibrous red P structure up to a certain depth into the TiO₂ nanotube arrays can be verified via Raman measurements. Therefore, TiO₂ nanotube membranes were cut along the cross section after CVD of fibrous red P, and imaging at specific spots from the surface of a TiO₂ nanotube array downward along a vertical line was acquired. The laser has a standard mode spot size of 1.5 μm (at 50× magnification). Raman spectra were recorded at several spots along the 65-μm-long cross section of the membranes. The experimental frequencies of bulk fibrous red P match the significant modes between 352 and 462 cm⁻¹ recorded up to 20 μm in distance to the surface from the top side and 15 μm in distance to the surface from the bottom side along the cross section of the membranes (shown in Figure S2). A systematic detection of spots further into the 65-μm-long tubes shows the

expected modes for pure anatase and the additional characteristic modes of fibrous P up to 15 μm recorded from the top side of the nanotube array and 15 μm from the bottom side (Figure 4). A reduction of the crystallinity of fibrous red P upon going deeper into the tubes can be observed.

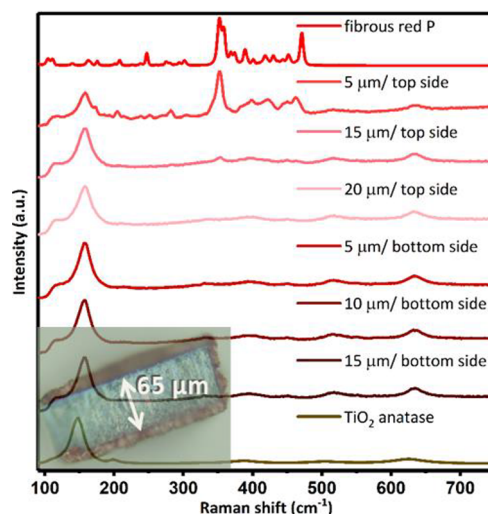


Figure 4. Raman spectroscopy on fibrous red P@TiO₂ membranes. From the top down: reference Raman spectrum of fibrous red P and spectra of a fibrous red P@TiO₂ membrane cross section measured at approximately 5, 15, and 20 μm in distance to the surface (membrane top side) and at approximately 5, 10, and 15 μm in distance to the surface (membrane bottom side) and a blank TiO₂ membrane (anatase, brown).

After the successful growth of fibrous red P onto and into TiO₂ nanotube arrays was demonstrated via powder XRD, SEM–EDS, Raman spectroscopy, and STEM–EDS analysis, the growth of partially crystalline fibrous P into the membrane was realized, whereas nicely crystallized fibrous P was found at the surface of the membranes.

Black P@TiO₂ Nanotubes. A similar successful gas-phase deposition has been performed with black P, another element allotrope of P. Black P is characterized by a structure (on the number of neighboring P layers)-dependent band-gap value covering a wide range of the electromagnetic spectrum.⁵¹ Thus, black P has potential in applications such as field-effect transistors, p–n junctions, photodetectors, etc.⁵² This orthorhombic allotrope of P crystallizes in space group *Cmca* (crystal structure in Figure 5a) shows a high carrier mobility and in-plane anisotropy, playing a role in hydrogen and oxygen generation in photocatalytic water splitting.⁵¹ Moreover, a broadening of the absorption fraction toward the visible-light range of 3.2 eV TiO₂ anatase can be provided by a heterojunction formation with the narrow-band-gap semiconductor black P. Depending on the number of neighboring layers stacked onto each other, a band gap of 0.3 eV in bulk black P to ~2 eV for the monolayer (called phosphorene) can be realized. The overall efficiency of the existing narrow-band-gap water-splitting photocatalysts is affected by photocorrosion, which results from the chemical bond strength of the given system.⁵³ This fact can be avoided by the fabrication of a heterojunction hybrid system between black P and TiO₂ nanotube arrays, where the chemical bond strength of the bulk material (TiO₂ anatase) will remain and only an alignment of the Fermi levels between the materials during charge-carrier

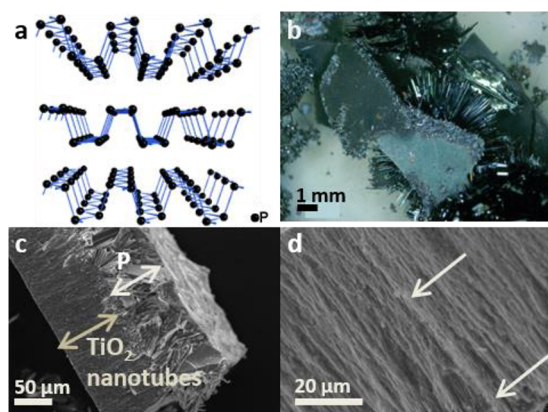


Figure 5. (a) Crystal structure of black P. (b) TiO₂ nanotube membranes with black P needles on the front and back sides after reaction via the gas phase. (c and d) SEM images of the cross section and covered surface of black P@TiO₂ nanotube membranes. There is visible horizontal growth along the vertical tube axis between white arrows. EDS of the cross section shows P all along the nanotubes.

transport reactions within the hybrid occurs.²³ A visual deposition of characteristic flat metallic-colored needles, spreading out gradually on the TiO₂ nanotube membranes (reversed side), can be seen in Figure 5b. A SEM image in Figure 5c shows the successful deposition of a thick black P layer covering the surface of this cut cross-sectional part of a TiO₂ nanotube membrane. The second SEM image in Figure 5d is displaying a gradual growth of small horizontally aligned black P crystals between the two arrows, which is confirmed by EDS measurements (Table S2). A reason for this unusual growth can be the unique 2D structure of black P. Powder XRD data can confirm the formation of black P on top of the TiO₂ nanotube arrays (Figure S3).

After separation of the TiO₂ nanotubes in an ultrasonication process, STEM imaging displays a singular tube with a width of ~150 nm. P was detected inside the tube besides Ti from the TiO₂ membrane after elemental mapping. Furthermore, analysis of tin (Sn) and iodine (I) inside the tubes was carried out because of the fact that SnI₄ was used during the transport reaction for synthesis. The formation of SnIP, as a possible side product, in such a transport reaction was ruled out (Figure 6).⁵⁰

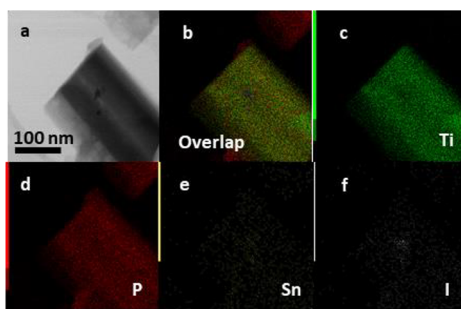


Figure 6. (a) STEM bright-field image of TiO₂ nanotubes separated from a membrane by an ultrasonication procedure. (b) Elemental mapping of overlaid elements Ti (representing TiO₂), P, Sn, and I. (c) Ti and (d) P substantiating P distributed along the full length of a TiO₂ nanotube, with (e) Sn and (f) I coming from the mineralizer only present in small amounts.

To verify the successful growth of black P into TiO₂ nanotubes, several Raman spectra were recorded after cutting the nanotube membranes at the cross section after synthesis. A simultaneous presence at the membrane surface of black P (main phase), with the most prominent modes at 360, 436, and 464 cm⁻¹ next to anatase with a characteristic mode at 145 cm⁻¹, can be confirmed. A gradual change is detectable when the laser is pointed down to a depth of 7 μm into the nanotubes, where black P next to anatase (main phase) still can be confirmed (Figure 7). The crystallinity of the black P phase

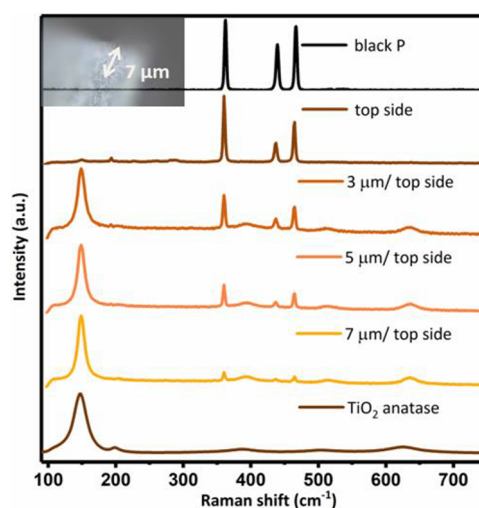


Figure 7. Raman spectroscopy on black P@TiO₂ membranes. From the top down: reference Raman spectrum of black P, spectra of a black P@TiO₂ membrane cross section measured at the surface and approximately 3, 5, and 7 μm in distance to the surface (membrane top side), and a fresh TiO₂ membrane (anatase, brown).

remains unchanged, in comparison to Raman imaging of fibrous red P@TiO₂ nanotubes. This is an additional proof of the assumption of distinct P needles in the SEM image in Figure 5d.

XPS. Characterization of the surface composition, binding energies, and oxidation states of fibrous red and black P next to blank TiO₂ samples, hybrid fibrous red P@TiO₂, and black P@TiO₂ was investigated via high-resolution XPS studies. The heterostructure systems reveal consistent oxidation states along with the pure samples. A shift of the binding energies in the O 1s region of fibrous red P@TiO₂ and black P@TiO₂ compared to pristine TiO₂ can be primarily attributed to the formation of P–O bonds in the heterostructure system (Figures S5 and S6).

UV–Vis Spectroscopy. The optical properties of the samples were determined using UV–vis in diffuse-reflectance mode (Figure S4). A sharp peak around 320 nm in the UV–vis spectrum of TiO₂ with a band tailing up to 380 nm arises from a O 2p → Ti 3d transition of electrons, demonstrating a VB to CB transition. The absorption spectrum of fibrous red P shows a broad absorption band extending to the visible range. Fibrous red P deposited on wide-band-gap TiO₂ shows improved absorption in the visible region because of the presence of moderate-band-gap fibrous red P. The UV–vis spectrum of black P shows three absorption bands at 315, 374, and 438 nm, with broadening of the absorption bands in the IR region. This is in line with findings in the published literature.^{54,55} After the deposition of black P on TiO₂ nanotubes, the visible-light and

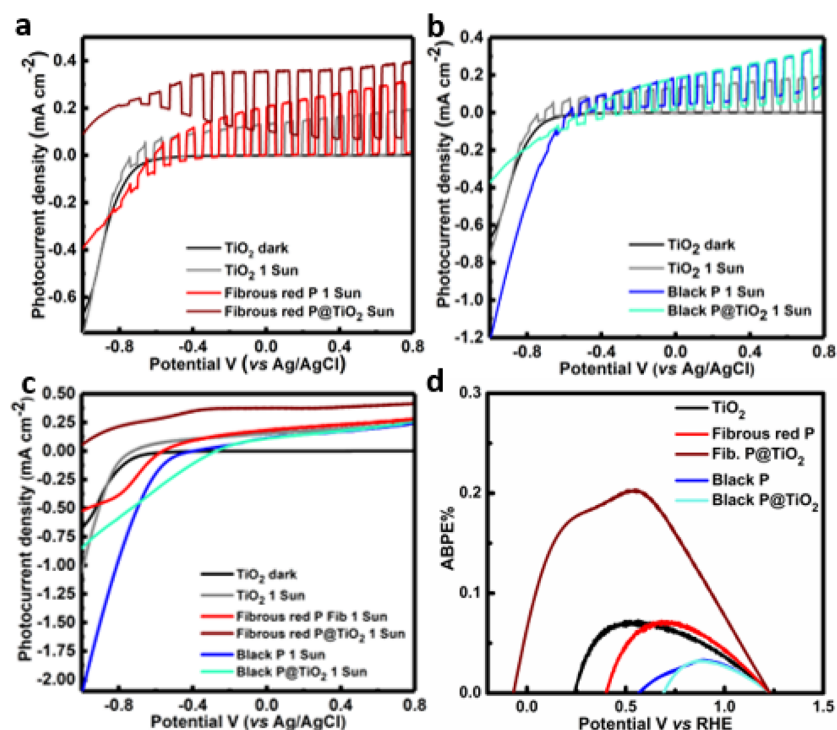


Figure 8. (a and b) Linear-sweep voltammograms of TiO₂, fibrous red P, fibrous red P@TiO₂, black P, and black P@TiO₂, under dark conditions and 1 solar simulated AM1.5 G light irradiation (100 mW cm⁻²) showing the photoresponse during on–off and (c) standard mode cycling. (d) ABPE % versus RHE plot under AM1.5 G light irradiation (100 mW cm⁻²). Color code: TiO₂ under dark conditions, black; TiO₂ under AM1.5 G light irradiation, grey; fibrous red P, red; fibrous red P@TiO₂, brown; black P, blue; black P@TiO₂, light blue.

IR absorption range was increased, which demonstrates a better visible-light response of the samples.

Visible-light absorption of the samples was investigated in detail using Tauc plots by plotting a graph of $(\alpha h\nu)^{1/2}$ versus $h\nu$, followed by extrapolation of a linear tangent to the X axis, where α is the absorption coefficient, h is the Planck constant, and ν is the light frequency (Figure S4). The values of the optical band gaps from the Tauc plots were found to be 2.97 eV for TiO₂, 1.97 eV for fibrous red P, 2.1 eV for fibrous red P@TiO₂, 1.67 eV for black P, and 1.54 eV for black P@TiO₂, respectively, which are in close agreement with the reported values and clearly demonstrate absorption in the visible region by the heterojunction hybrids (Figure S4).

Photocatalytic Activity of P Allotrope@TiO₂ Nanotube Hybrids. The photoelectrochemical water splitting performance of all compounds was tested using a three-electrode system. In this setup, the specimens, deposited on fluorine-doped tin oxide, formed the anode (working electrode), while platinum and Ag/AgCl were used as the cathodes (counter electrode) and reference electrode, respectively. The photoanode was irradiated with AM1.5 G simulated sunlight with a power density of 100 mW cm⁻² (1 sun) at the sample surface. The current density (mA cm⁻²) was measured using linear-sweep voltammetry (LSV) by sweeping the applied voltage from -0.1 to $+0.8$ V versus Ag/AgCl at a scan rate of 0.1 V s⁻¹. To compare the photoresponses, the dark current was also measured. The photocurrent response during light on–off cycles shows a rise and drop in the photocurrent, which substantiates the photogeneration of charge carriers in the samples under light irradiation (Figure 8a,b). The photocurrent densities for TiO₂, fibrous red P, fibrous red P@TiO₂, black P, and black P@TiO₂, at 0.6 V versus Ag/AgCl (1.23 V vs RHE; water oxidation

potential), were measured to be 0.22 , 0.25 , 0.60 , 0.19 , and 0.20 mA cm⁻² respectively (Figure 8c). Under dark conditions, a negligible current was observed. The photocurrent densities of pristine black P, bare TiO₂, and pristine fibrous red P were almost identical because of the poor carrier separation in P and the lack of visible-light absorption in TiO₂. Further, black P@TiO₂ does not show a noticeable increase in the photocurrent density, which can be attributed to the lack of a synergistic photocatalytic process, which is likely due to the higher degree of oxidation of P in black P to P_xO_y, which was evident in the XPS data (Figure S5). Interestingly, the fibrous red P@TiO₂ hybrid exhibited a relatively high photocurrent density (0.60 mA cm⁻²), suggesting the successful formation of a heterojunction and better charge transfer between fibrous red P and TiO₂ (Figure 8a). The viability of the photocatalytic system to perform under visible light was tested by irradiating the specimens with a 425 nm LED light and a power density of 54.15 mW cm⁻². The increase in the photocurrent under 425 nm of irradiation clearly demonstrates the applicability of the system to perform at longer wavelengths (Figure S11). The highest applied bias photon-to-current efficiency percentage (ABPE %; calculation details are given in the SI) was found for a fibrous red P@TiO₂ nanohybrid, which was approximately 3.0 times higher than that for TiO₂ and pristine fibrous red P, and demonstrates that heterojunction formation with TiO₂ increases the photoelectrocatalytic performance significantly (Figure 8d).^{56,57} Further, action spectra, showing IPCE and APCE % of materials as a function of the wavelength, demonstrate that a fibrous red P@TiO₂ nanohybrid outperformed and calculated IPCE and APCE % at 450 nm were found to be 1.30 and 1.65% , respectively (see the SI). To verify that the generated photocurrent originated from the photoelectrochemical water splitting and not from side reactions or

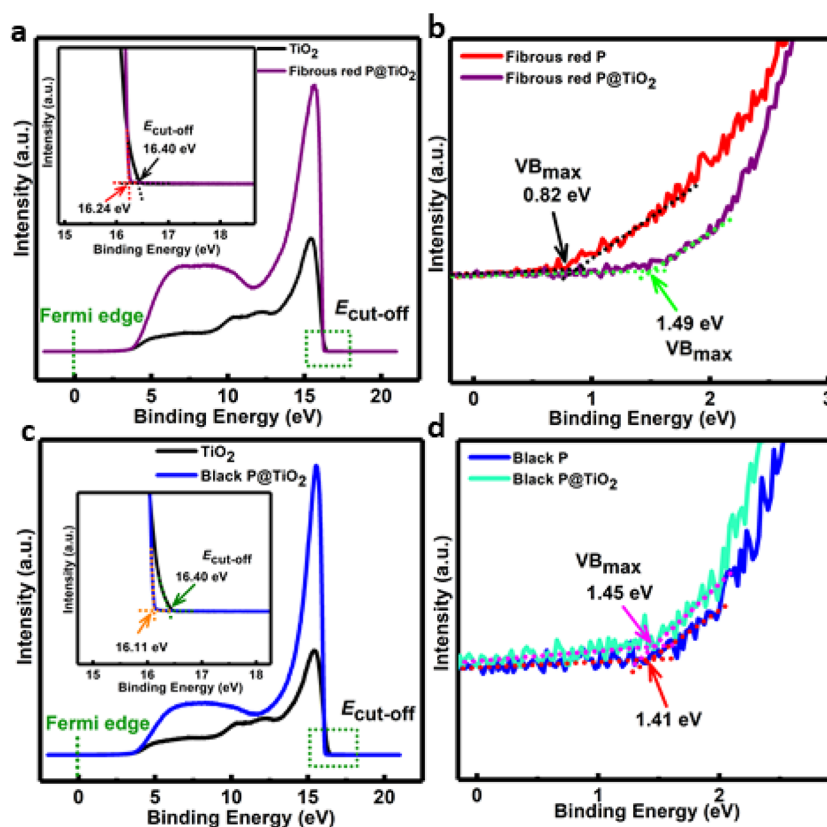


Figure 9. UPS WF spectra of (a) TiO_2 and fibrous red P@TiO_2 and (c) TiO_2 and black P@TiO_2 . Inset: $E_{\text{cut-off}}$. The value of the WF was determined from the UPS WF spectra by using the equation $\text{WF}(\Phi) = 21.21 - E_{\text{cut-off}}$, where 21.21 eV is the energy of the incident He I line of a He discharge lamp used for UPS. UPS VB spectra of (b) fibrous red P and fibrous red P@TiO_2 and (d) black P and black P@TiO_2 . Color code: TiO_2 , black; fibrous red P, red; fibrous red P@TiO_2 , purple; black P, blue; black P@TiO_2 , light blue.

photocorrosion of the electrodes, evolved hydrogen at the platinum counter electrode was collected to calculate the Faradaic efficiency (FE; see section 2.6 in the SI). The black P@TiO_2 hybrid displayed the highest FE (90.61%), demonstrating the origin of the photocurrent from water splitting and negligible photocorrosion of the materials.

The band-edge energies with respect to the vacuum levels of all samples were determined from the work function (WF) and VB spectra acquired using ultraviolet photoelectron spectroscopy (UPS; Figure 9). The WF was calculated by subtracting the energy of the emitted secondary electrons (cutoff energy $E_{\text{cut-off}}$) from the energy of the incident UV light (He I line of a He discharge lamp: 21.21 eV) using the expression $\text{WF}(\Phi) = 21.21 - E_{\text{cut-off}}$. The extrapolation of the linear region of the WF spectrum on the X and Y scales and their point of intersection gave the value of the cutoff energy. The $E_{\text{cut-off}}$ values of TiO_2 , fibrous red P@TiO_2 , and black P@TiO_2 were found to be 16.40, 16.24, and 16.11 eV, respectively. Hence, the values of WF were calculated to be 4.81, 4.97, and 5.10 eV (Figure 9a,c and insets). The increase of the WF value demonstrates depletion region formation with concomitant band bending at the solid-state heterointerface, which leads to a deepening of the Fermi level of TiO_2 in P@TiO_2 hybrids. Additionally, the valence-band maximum (VB_{max}) values calculated via linear extrapolation of the leading edges of the UPS VB spectra for fibrous red P, fibrous red P@TiO_2 , black P, and black P@TiO_2 were found to be 0.82, 1.49, 1.41, and 1.45 eV below the Fermi level. The small difference in the energies between the Fermi level and VB_{max} ($E_{\text{F}} - E_{\text{VB}_{\text{max}}}$) for fibrous red P (0.82 eV) and

black P (1.41 eV) reveals that the Fermi level was close to VB_{max} and the samples were moderately p-type. Further, XPS VB spectra of TiO_2 gave the value of VB_{max} as 3.15 eV below the Fermi level (Figure S4). The increase in VB_{max} in black P@TiO_2 and fibrous red P@TiO_2 implies a slightly uplifted Fermi level of P in the heterojunction during Fermi-level alignment and band bending (Figure 10). From the WF and VB_{max} results, it can be concluded that heterojunction formation between P and TiO_2 was facilitated by upward band bending in TiO_2 and downward band bending in P allotropes (black P and fibrous red P), as expected for a p–n heterojunction. Further, surface potential measurement of materials under dark and light conditions provides evidence of Fermi-level alignment and better charge transport due to the formation of a heterojunction (see section 2.8 in the SI for more details).

Plausible Mechanism. The water-splitting process proceeds via the absorption of light by the semiconductors, generating electron–hole pairs, which drive proton reduction and water oxidation reactions. In photoelectrochemical water splitting, electrons in the CB of the semiconductors move toward the platinum cathode, where they reduce protons, while holes in the VB of the semiconductors oxidize water to produce oxygen at the anode. Wide band gaps (>1.23 eV) and aligned positions of the CB and VB (CB < 0.00 eV and VB > +1.23 eV vs NHE at pH 0) are required to achieve proton reduction and water oxidation, respectively. TiO_2 has a large band gap, and electron–hole pairs can only be produced under UV irradiation, which demonstrates the origin of very small photocurrent density in LSV. However, from DR UV–vis, the

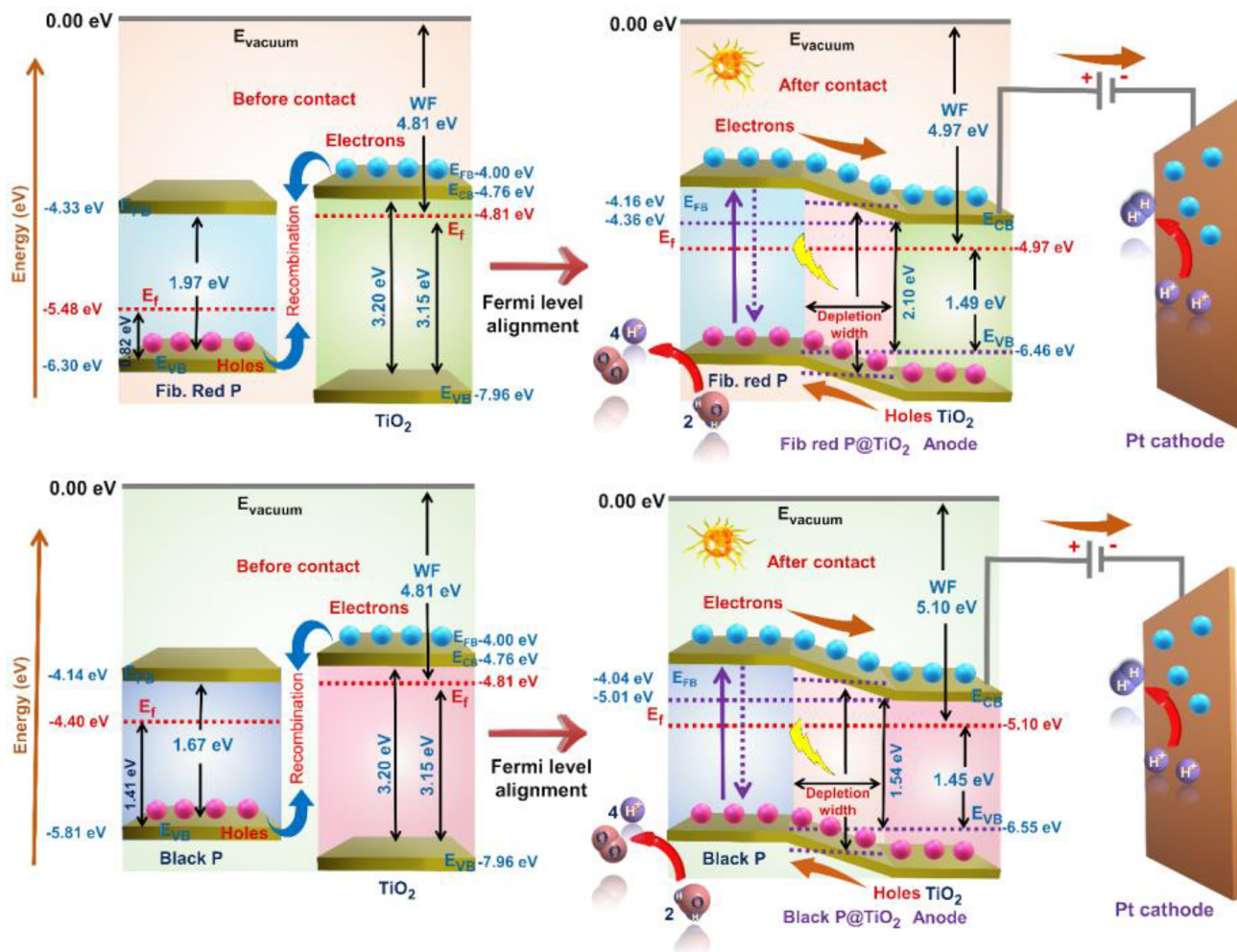


Figure 10. Energy-level diagrams illustrating a plausible charge-separation mechanism in P allotrope@TiO₂ heterojunctions.

value of the optical band gap was found to be 2.97 eV, which corresponds to 417 nm; in other words, a small visible-light fraction can be absorbed by TiO₂. The decrease in the band gap of TiO₂ might be explained as the presence of a few Ti³⁺ defects, oxygen vacancies, and trap sites. Moreover, because of the low band gaps of pristine black P and fibrous red P, the generation of sufficient reductive and oxidative electrons and holes to facilitate the water-splitting reaction can be affected.^{58,59} However, a hybrid material, consisting of fibrous red P with TiO₂, was found to be an efficient photocatalyst as a result of the formation of a heterojunction and efficient charge transfer between fibrous red P and TiO₂. Heterojunction formation leads to Fermi-level alignment. During Fermi-level alignment, electrons flow from one semiconductor to another, which equilibrates the Fermi-level position between the semiconductors. Measurements of the flat-band potential for TiO₂, pristine fibrous red P, and black P were carried out via Mott–Schottky analysis (Figure S12b), and the positions were found to be -0.70 , -0.37 , and -0.56 V versus Ag/AgCl (-4.00 , -4.14 , and -4.33 eV on the E_{vac} scale); however, we note that the n-type behavior found for pristine fibrous red P and black P is attributed to a compact TiO₂ layer used during measurements and should be discounted. This indicates an electron transfer from TiO₂ to black P or fibrous red P, respectively, during Fermi-level alignment. After hybrid heterojunction formation and equilibrium was reached, the

positions of the flat-band potentials of fibrous red P@TiO₂ and black P@TiO₂ were found to be -0.54 and -0.66 V versus Ag/AgCl (-4.16 and -4.04 eV at the E_{vac} scale; Figure 10). The downshifting of the flat-band potential of TiO₂ in hybrid systems suggests downward band bending of the CB edge of fibrous red and black P while upward band bending in TiO₂ occurs. This clearly demonstrates the formation of a p–n-type heterojunction between P allotropes and TiO₂. These observations were also supported by WF values (position of the Fermi level in a vacuum), where the WF of TiO₂ changed from 4.97 versus vacuum in fibrous red P@TiO₂ to 4.81–5.10 eV in black P@TiO₂ (Figure 10), which is a sufficiently positive potential for water oxidation to occur (-5.72 eV vs E_{vac} or $+1.23$ V vs NHE at pH 0). The increase in the WF value in hybrid materials demonstrates lower shifting of the Fermi level, which agrees well with heterojunction formation.

Additionally, a deeper V_{Bmax} in hybrid P allotrope@TiO₂ compounds than in pristine P allotropes suggests the successful formation of a heterojunction and generation of more oxidative holes to facilitate water splitting. On the basis of the above findings, we have sketched a band-structure diagram of the hybrid materials, which demonstrates that more efficient water splitting was possible because of p–n heterojunction formation and better charge separation (Figure 10). Further, Nyquist plots demonstrate that charge-transfer resistance and charge-transport resistance of hybrids are lower in comparison to

pristine TiO₂, which suggests better charge transfer and transport in hybrid materials (Figure S12). The cavities of the TiO₂ nanotube membranes are evidently filled with visible-light-absorbing P allotropes. Thus, generated electron–hole pairs can be transferred to TiO₂. Because of a short path distance and TiO₂ exhibiting a high carrier mobility, carrier recombination can be prevented and a fast transit of the charge carriers toward the semiconductor–electrolyte interface is enabled.

CONCLUSION

Hybrid heterojunction systems for optoelectronic applications were designed, fabricated, characterized, and tested. The so-called mineralization principle for short-way gas-phase transport of solids was performed to grow semiconductors on TiO₂ nanotube arrays. Fibrous red and black P were successfully deposited onto and into electrochemically produced TiO₂ nanotube membranes. The formation of hybrid nanostructures was analyzed with several spectroscopic and diffraction methods such as XRD, STEM–EDS, Raman spectroscopy, UV–vis, and XPS. The effectiveness of the vapor transport was verified through SEM, STEM, and elemental mapping of the surface and cross section of nanohybrids, showing deposition of the materials inside the tubes.

Raman spectroscopy taken at the surface and along the razor-cut cross section of the nanotubes confirmed the penetration and growth of fibrous red P up to 15 μm (65 μm in length) and black P up to 7 μm into the nanotubes (60 μm in length). The fibrous red P@TiO₂ and black P@TiO₂ hybrid materials displayed an improved photoelectrochemical performance for water splitting in the visible-light regime because of successful p–n heterojunction formation. UPS WF spectra demonstrate band alignment, the Fermi level of TiO₂ gets downshifted, and an upshift was observed for the P allotropes during heterojunction formation. This formation enables carrier transportation from the VB of downshifted TiO₂ to P allotropes, resulting in successful oxidation in the water splitting. At the same time, Mott–Schottky plots corroborate the occurrence of more reductive flat bands in hybrid P allotrope@TiO₂ materials, which facilitate the effective reduction of hydrogen. The increased charge-carrier mobility, lower charge-transfer resistance, and lower charge-transport resistance of such hybrid materials lead to better charge separation and an improved photoelectrochemical performance.

ASSOCIATED CONTENT

Supporting Information

The Supporting Information is available free of charge on the ACS Publications website at DOI: 10.1021/acsanm.9b00221.

Experimental details on the synthesis and physicochemical and photoelectrochemical characterization, additional characterization on powder XRD, Raman and EDS analyses, DR UV–vis, high-resolution XPS, photocurrent density, electrochemical impedance spectroscopy, Nyquist and Mott–Schottky plots, and XPS VB spectra (PDF)

AUTHOR INFORMATION

Corresponding Authors

*E-mail: kshankar@ualberta.ca.

*E-mail: tom.nilges@lrz.tum.de.

ORCID

Pawan Kumar: 0000-0003-2804-9298

Ryan Kisslinger: 0000-0003-2456-396X

Karthik Shankar: 0000-0001-7347-3333

Tom Nilges: 0000-0003-1415-4265

Author Contributions

[§]These authors contributed equally.

Author Contributions

E.Ü. and R.K. performed the synthesis and characterization of P/hybrid materials. P.Ku. was involved in the XPS, UPS, and photoelectrochemical studies and compiled the results. P.Ka. performed the electrochemical characterizations. K.S. and T.N. planned and supervised the research. All authors were involved in writing their respective parts.

Notes

The authors declare no competing financial interest.

ACKNOWLEDGMENTS

This work has been performed as part of the international graduate school ATUMS (IRTG 2022) funded by Deutsche Forschungsgemeinschaft and Natural Sciences and Engineering Research Council of Canada (NSERC). The performance and assistance in STEM–EDS by Peng Li, Shihong Xu, and Anqiang He from nanoFAB at the University of Alberta are gratefully acknowledged. We thank Anna Vogel for Raman spectroscopy of the samples. K.S. acknowledges NSERC, National Research Council Canada, Future Energy Systems (FES), and CMC Microsystems for research funding and allowances for tool usage. P.Ku. is thankful to FES for a postdoctoral research fellowship. We kindly acknowledge Dr. Kazi Alam for DR UV–vis measurements.

ABBREVIATIONS

black P@TiO₂ = hybrid of black phosphorus and TiO₂

CB = conduction band

DR UV–vis = diffuse-reflectance ultraviolet–visible spectroscopy

fibrous red P@TiO₂ = hybrid of fibrous red phosphorus and TiO₂

IR = infrared radiation

KPFM = Kelvin probe force microscopy

LSV = linear sweep voltammetry

NHE = normal hydrogen electrode

SEM = scanning electron microscopy

STEM–EDS = scanning transmission electron microscopy–energy-dispersive X-ray spectroscopy

VB = valence band

UPS = ultraviolet photoelectron spectroscopy

WF = work function

XPS = X-ray photoelectron spectroscopy

XRD = X-ray diffraction

REFERENCES

- (1) Yuan, Y.-P.; Ruan, L.-W.; Barber, J.; Joachim Loo, S. C.; Xue, C. Hetero-nanostructured suspended photocatalysts for solar-to-fuel conversion. *Energy Environ. Sci.* **2014**, *7*, 3934–3951.
- (2) Liao, L.; Su, Z.; Wang, Y.; Li, Y.; Lu, X.; Zhang, Q.; Zhao, Z.; Wei, D.; Feng, G.; Yu, Q.; Cai, X.; Baldelli, S.; Zhao, J.; Ren, Z.; Fang, H.; Robles-Hernandez, F.; Bao, J. Efficient solar water-splitting using a nanocrystalline CoO photocatalyst. *Nat. Nanotechnol.* **2014**, *9*, 69–73.
- (3) Liu, J.; Liu, Y.; Liu, N.; Han, Y.; Zhang, X.; Huang, H.; Lifshitz, Y.; Lee, S.-T.; Zhong, J.; Kang, Z. Metal-free efficient photocatalyst for

stable visible water splitting via a two-electron pathway. *Science* **2015**, *347*, 970–974.

(4) Roger, I.; Shipman, M. A.; Symes, M. D. Earth-abundant catalysts for electrochemical and photoelectrochemical water splitting. *Nat. Rev. Chem.* **2017**, *1*, 0003.

(5) Maeda, K.; Teramura, K.; Lu, D.; Takata, T.; Saito, N.; Inoue, Y.; Domen, K. Photocatalyst releasing hydrogen from water. *Nature* **2006**, *440*, 295.

(6) Sun, Y.; Cheng, H.; Gao, S.; Sun, Z.; Liu, Q.; Liu, Q.; Lei, F.; Yao, T.; He, J.; Wei, S.; Xie, Y. Freestanding tin disulfide single-layers realizing efficient visible-light water splitting. *Angew. Chem.* **2012**, *124*, 8857–8861.

(7) Wang, Q.; Hisatomi, T.; Jia, Q.; Tokudome, H.; Zhong, M.; Wang, C.; Pan, Z.; Takata, T.; Nakabayashi, M.; Shibata, N.; Li, Y.; Sharp, I. D.; Kudo, A.; Yamada, T.; Domen, K. Scalable water splitting on particulate photocatalyst sheets with a solar-to-hydrogen energy conversion efficiency exceeding 1%. *Nat. Mater.* **2016**, *15*, 611.

(8) Habisreutinger, S. N.; Schmidt-Mende, L.; Stolarczyk, J. K. Photocatalytic reduction of CO₂ on TiO₂ and other semiconductors. *Angew. Chem., Int. Ed.* **2013**, *52*, 7372–7408.

(9) Sheridan, M. V.; Hill, D. J.; Sherman, B. D.; Wang, D.; Marquard, S. L.; Wee, K.-R.; Cahoon, J. F.; Meyer, T. J. All-in-One Derivatized Tandem p+n-Silicon–SnO₂/TiO₂ Water Splitting Photoelectrochemical Cell. *Nano Lett.* **2017**, *17*, 2440–2446.

(10) Moniz, S. J.; Shevlin, S. A.; Martin, D. J.; Guo, Z.-X.; Tang, J. Visible-light driven heterojunction photocatalysts for water splitting—a critical review. *Energy Environ. Sci.* **2015**, *8*, 731–759.

(11) Jaafar, S. N. H.; Minggu, L. J.; Arifin, K.; Kassim, M. B.; Wan, W. R. D. Natural dyes as TiO₂ sensitizers with membranes for photoelectrochemical water splitting: An overview. *Renewable Sustainable Energy Rev.* **2017**, *78*, 698–709.

(12) Ge, M.; Li, Q.; Cao, C.; Huang, J.; Li, S.; Zhang, S.; Zhang, K.; Lai, Y.; Chen, Z.; Al-Deyab, S. S. One-dimensional TiO₂ Nanotube Photocatalysts for Solar Water Splitting. *Adv. Sci.* **2017**, *4*, 1600152.

(13) Park, J. H.; Kim, S.; Bard, A. J. Novel carbon-doped TiO₂ nanotube arrays with high aspect ratios for efficient solar water splitting. *Nano Lett.* **2006**, *6*, 24–28.

(14) Pu, Y.-C.; Wang, G.; Chang, K.-D.; Ling, Y.; Lin, Y.-K.; Fitzmorris, B. C.; Liu, C.-M.; Lu, X.; Tong, Y.; Zhang, J. Z.; Hsu, Y.-J.; Li, Y. Au nanostructure-decorated TiO₂ nanowires exhibiting photoactivity across entire UV-visible region for photoelectrochemical water splitting. *Nano Lett.* **2013**, *13*, 3817–3823.

(15) Lee, C. Y.; Taylor, A. C.; Beirne, S.; Wallace, G. G. 3D-Printed Conical Arrays of TiO₂ Electrodes for Enhanced Photoelectrochemical Water Splitting. *Adv. Energy Mater.* **2017**, *7*, 1701060.

(16) de Brito, J. F.; Tavella, F.; Genovese, C.; Ampelli, C.; Zaroni, M. V. B.; Centi, G.; Perathoner, S. Role of CuO in the modification of the photocatalytic water splitting behavior of TiO₂ nanotube thin films. *Appl. Catal., B* **2018**, *224*, 136–145.

(17) Ning, X.; Li, J.; Yang, B.; Zhen, W.; Li, Z.; Tian, B.; Lu, G. Inhibition of photocorrosion of CdS via assembling with thin film TiO₂ and removing formed oxygen by artificial gill for visible light overall water splitting. *Appl. Catal., B* **2017**, *212*, 129–139.

(18) Mor, G. K.; Shankar, K.; Paulose, M.; Varghese, O. K.; Grimes, C. A. Use of highly-ordered TiO₂ nanotube arrays in dye-sensitized solar cells. *Nano Lett.* **2006**, *6*, 215–218.

(19) Mor, G. K.; Varghese, O. K.; Paulose, M.; Shankar, K.; Grimes, C. A. A review on highly ordered, vertically oriented TiO₂ nanotube arrays: Fabrication, material properties, and solar energy applications. *Sol. Energy Mater. Sol. Cells* **2006**, *90*, 2011–2075.

(20) Wang, F.; Ng, W. K. H.; Yu, J. C.; Zhu, H.; Li, C.; Zhang, L.; Liu, Z.; Li, Q. Red phosphorus: an elemental photocatalyst for hydrogen formation from water. *Appl. Catal., B* **2012**, *111–112*, 409–414.

(21) Kudo, A.; Miseki, Y. Heterogeneous photocatalyst materials for water splitting. *Chem. Soc. Rev.* **2009**, *38*, 253–278.

(22) Roy, P.; Berger, S.; Schmuki, P. TiO₂ nanotubes: synthesis and applications. *Angew. Chem., Int. Ed.* **2011**, *50*, 2904–2939.

(23) Schock, H.; Meissner, D., *Solarzellen-Physikalische Grundlagen und Anwendungen in der Photovoltaik*; Vieweg & Sohn: Wiesbaden, Germany, 1993.

(24) Regonini, D.; Bowen, C. R.; Jaroenworarluck, A.; Stevens, R. A review of growth mechanism, structure and crystallinity of anodized TiO₂ nanotubes. *Mater. Sci. Eng., R* **2013**, *74*, 377–406.

(25) Hahn, R.; Macak, J.; Schmuki, P. Rapid anodic growth of TiO₂ and WO₃ nanotubes in fluoride free electrolytes. *Electrochem. Commun.* **2007**, *9*, 947–952.

(26) Ravi, P.; Navakoteswara Rao, V.; Shankar, M.; Sathish, M. CuO/Cr₂O₃ core-shell structured co-catalysts on TiO₂ for efficient photocatalytic water splitting using direct solar light. *Int. J. Hydrogen Energy* **2018**, *43*, 3976–3987.

(27) Keyes, R. W. The electrical properties of black phosphorus. *Phys. Rev.* **1953**, *92*, 580.

(28) Morita, A. Semiconducting black phosphorus. *Appl. Phys. A: Solids Surf.* **1986**, *39*, 227–242.

(29) Yan, J.; Ji, Y.; Kong, L.; Li, Y.; Navlani-García, M.; Liu, S.; Kuwahara, Y.; Mori, K.; Che, M.; Yamashita, H. Black Phosphorus-Based Compound with Few Layers for Photocatalytic Water Oxidation. *ChemCatChem* **2018**, *10*, 3424–3428.

(30) Li, L.; Yu, Y.; Ye, G. J.; Ge, Q.; Ou, X.; Wu, H.; Feng, D.; Chen, X. H.; Zhang, Y. Black phosphorus field-effect transistors. *Nat. Nanotechnol.* **2014**, *9*, 372.

(31) Yuan, H.; Liu, X.; Afshinmanesh, F.; Li, W.; Xu, G.; Sun, J.; Lian, B.; Curto, A. G.; Ye, G.; Hikita, Y.; Shen, Z.; Zhang, S.-C.; Chen, X.; Brongersma, M.; Hwang, H. Y.; Cui, Y. Polarization-sensitive broadband photodetector using a black phosphorus vertical p–n junction. *Nat. Nanotechnol.* **2015**, *10*, 707.

(32) Viti, L.; Hu, J.; Coquillat, D.; Knap, W.; Tredicucci, A.; Politano, A.; Vitiello, M. S. Black-phosphorus Terahertz photodetectors. *Adv. Mater.* **2015**, *27*, 5567–5572.

(33) Zhou, Y.; Zhang, Y.; Lin, M.; Long, J.; Zhang, Z.; Lin, H.; Wu, J. C.-S.; Wang, X. Monolayered Bi₂WO₆ nanosheets mimicking heterojunction interface with open surfaces for photocatalysis. *Nat. Commun.* **2015**, *6*, 8340.

(34) Chen, S.; Qi, Y.; Hisatomi, T.; Ding, Q.; Asai, T.; Li, Z.; Ma, S. S. K.; Zhang, F.; Domen, K.; Li, C. Efficient Visible Light-Driven Z-Scheme Overall Water Splitting Using a MgTa₂O_{6-x}N_y/TaON Heterostructure Photocatalyst for H₂ Evolution. *Angew. Chem.* **2015**, *127*, 8618–8621.

(35) Shang, L.; Tong, B.; Yu, H.; Waterhouse, G. I. N.; Zhou, C.; Zhao, Y.; Tahir, M.; Wu, L.-Z.; Tung, C.-H.; Zhang, T. CdS Nanoparticle-Decorated Cd Nanosheets for Efficient Visible Light-Driven Photocatalytic Hydrogen Evolution. *Adv. Energy Mater.* **2016**, *6*, 1501241.

(36) Nguyen, C. C.; Vu, N. N.; Do, T.-O. Recent advances in the development of sunlight-driven hollow structure photocatalysts and their applications. *J. Mater. Chem. A* **2015**, *3*, 18345–18359.

(37) Lewis, N. S. Toward cost-effective solar energy use. *Science* **2007**, *315*, 798–801.

(38) Zhang, X.; Han, F.; Shi, B.; Farsinezhad, S.; Dechaine, G. P.; Shankar, K. Photocatalytic conversion of diluted CO₂ into light hydrocarbons using periodically modulated multiwalled nanotube arrays. *Angew. Chem., Int. Ed.* **2012**, *51*, 12732–12735.

(39) Mohammadpour, A.; Kar, P.; Wiltshire, B. D.; Askar, A. M.; Shankar, K. Electron transport, trapping and recombination in anodic TiO₂ nanotube arrays. *Curr. Nanosci.* **2015**, *11*, 593–614.

(40) Macak, J.; Barczuk, P.; Tsuchiya, H.; Nowakowska, M.; Ghicov, A.; Chojak, M.; Bauer, S.; Virtanen, S.; Kulesza, P.; Schmuki, P. Self-organized nanotubular TiO₂ matrix as support for dispersed Pt/Ru nanoparticles: Enhancement of the electrocatalytic oxidation of methanol. *Electrochem. Commun.* **2005**, *7*, 1417–1422.

(41) Paramasivam, I.; Macak, J.; Ghicov, A.; Schmuki, P. Enhanced photochromism of Ag loaded self-organized TiO₂ nanotube layers. *Chem. Phys. Lett.* **2007**, *445*, 233–237.

(42) Yang, G.; Chen, D.; Ding, H.; Feng, J.; Zhang, J. Z.; Zhu, Y.; Hamid, S.; Bahnemann, D. W. Well-designed 3D ZnIn₂S₄ nanosheets/TiO₂ nanobelts as direct Z-scheme photocatalysts for CO₂

photoreduction into renewable hydrocarbon fuel with high efficiency. *Appl. Catal., B* **2017**, *219*, 611–618.

(43) Zhou, D.; Chen, Z.; Yang, Q.; Shen, C.; Tang, G.; Zhao, S.; Zhang, J.; Chen, D.; Wei, Q.; Dong, X. Facile Construction of g-C₃N₄ Nanosheets/TiO₂ Nanotube Arrays as Z-Scheme Photocatalyst with Enhanced Visible-Light Performance. *ChemCatChem* **2016**, *8*, 3064–3073.

(44) Pi, Y.; Li, Z.; Xu, D.; Liu, J.; Li, Y.; Zhang, F.; Zhang, G.; Peng, W.; Fan, X. 1T-Phase MoS₂ Nanosheets on TiO₂ Nanorod Arrays: 3D Photoanode with Extraordinary Catalytic Performance. *ACS Sustainable Chem. Eng.* **2017**, *5*, 5175–5182.

(45) Qin, P.; Paulose, M.; Dar, M. I.; Moehl, T.; Arora, N.; Gao, P.; Varghese, O. K.; Grätzel, M.; Nazeeruddin, M. K. Stable and efficient perovskite solar cells based on titania nanotube arrays. *Small* **2015**, *11*, 5533–5539.

(46) Thakur, U.; Kisslinger, R.; Shankar, K. One-dimensional electron transport layers for perovskite solar cells. *Nanomaterials* **2017**, *7*, 95.

(47) Lou, Z.; Li, F.; Deng, J.; Wang, L.; Zhang, T. Branch-like hierarchical heterostructure (α -Fe₂O₃/TiO₂): a novel sensing material for trimethylamine gas sensor. *ACS Appl. Mater. Interfaces* **2013**, *5*, 12310–12316.

(48) Eckstein, N.; Hohmann, A.; Wehrich, R.; Nilges, T.; Schmidt, P. Synthesis and Phase Relations of Single-Phase Fibrous Phosphorus. *Z. Anorg. Allg. Chem.* **2013**, *639*, 2741–2743.

(49) Grotz, C.; Köpf, M.; Baumgartner, M.; Jantke, L. A.; Raudasch-Sieber, G.; Fässler, T. F.; Nilges, T. Synthesis, Structure, and Properties of NaP₇, a Phosphorus-rich Polyphosphide. *Z. Anorg. Allg. Chem.* **2015**, *641*, 1395–1399.

(50) Pfister, D.; Schaefer, K.; Ott, C.; Gerke, B.; Poettgen, R.; Janka, O.; Baumgartner, M.; Efimova, A.; Hohmann, A.; Schmidt, P.; Venkatachalam, S.; van Wuelen, L.; Schuermann, U.; Kienle, L.; Duppel, V.; Parzinger, E.; Miller, B.; Becker, J.; Holleitner, A.; Wehrich, R.; Nilges, T. Inorganic Double Helices in Semiconducting SnIP. *Adv. Mater.* **2016**, *28*, 9783–9791.

(51) Castellanos-Gomez, A. Black phosphorus: narrow gap, wide applications. *J. Phys. Chem. Lett.* **2015**, *6*, 4280–4291.

(52) Abbas, A. N.; Liu, B.; Chen, L.; Ma, Y.; Cong, S.; Aroonyadet, N.; Köpf, M.; Nilges, T.; Zhou, C. Black phosphorus gas sensors. *ACS Nano* **2015**, *9*, 5618–5624.

(53) Grätzel, M. Photoelectrochemical cells. *Nature* **2001**, *414*, 338.

(54) Guo, Z.; Zhang, H.; Lu, S.; Wang, Z.; Tang, S.; Shao, J.; Sun, Z.; Xie, H.; Wang, H.; Yu, X. F.; Chu, P. K. From black phosphorus to phosphorene: basic solvent exfoliation, evolution of Raman scattering, and applications to ultrafast photonics. *Adv. Funct. Mater.* **2015**, *25*, 6996–7002.

(55) Wang, H.; Yang, X.; Shao, W.; Chen, S.; Xie, J.; Zhang, X.; Wang, J.; Xie, Y. Ultrathin black phosphorus nanosheets for efficient singlet oxygen generation. *J. Am. Chem. Soc.* **2015**, *137*, 11376–11382.

(56) Chen, Z.; Dinh, H. N.; Miller, E. *Photoelectrochemical Water Splitting*; Springer: Berlin, 2013.

(57) Zhang, X.; Zhang, B.; Cao, K.; Brillet, J.; Chen, J.; Wang, M.; Shen, Y. A perovskite solar cell-TiO₂@BiVO₄ photoelectrochemical system for direct solar water splitting. *J. Mater. Chem. A* **2015**, *3*, 21630–21636.

(58) Hoang, S.; Berglund, S. P.; Hahn, N. T.; Bard, A. J.; Mullins, C. B. Enhancing visible light photo-oxidation of water with TiO₂ nanowire arrays via cotreatment with H₂ and NH₃: synergistic effects between Ti³⁺ and N. *J. Am. Chem. Soc.* **2012**, *134*, 3659–3662.

(59) Chen, X.; Liu, L.; Yu, P. Y.; Mao, S. S. Increasing solar absorption for photocatalysis with black hydrogenated titanium dioxide nanocrystals. *Science* **2011**, *331*, 746–750.